Physical weathering of carbonate host-rock by precipitation of soluble salts in caves: a case study in El Orón-Arco Cave (Region of Murcia, SE Spain)

Fernando Gázquez[(1)*], José-María Calaforra[(1)], Nicholas P. Evans[(2)], Alexandra V. Turchyn[(2)], Fernando Rull[(3)], Jesús Medina[(3)], Andrés Ros[(4)], José Luis Llamusí[(4)], Juan Sánchez[(4)] and David A. Hodell[(2)]

(1) Department of Biology and Geology, Universidad de Almería, Carretera de Sacramento s.n, La Cañada de San Urbano, Almería, 04120, Spain.

(2) Department of Earth Sciences, University of Cambridge, Downing Street, Cambridge, CB2 3EQ, United Kingdom.

(3) Departamento de Física de la Materia Condensada, Cristalografía y Mineralogía. Universidad de Valladolid. Paseo de Belén, 7, 47011, Valladolid, Spain

(4) Centro de Estudios Ambientales y del Mar. CENM-naturaleza, Alcántara, 5, Cartagena, Murcia, 30394, Spain.

*corresponding author (f.gazquez@ual.es)

ABSTRACT

The dissolution of carbonate host-rock by freshwater in phreatic or vadose conditions is the most common mechanism for the formation of caves; however, circulation of saline solutions through carbonate materials and precipitation of soluble salts may also play an important role. We studied the stable isotope composition ($\delta^{18}O$ and $\delta^{34}S$ of sulfate, $\delta^{18}O$ and δD of structurally-bound gypsum hydration water and $^{87}Sr/^{86}Sr$) and salinity of fluid inclusions in gypsum speleothems found in El Orón-Arco Cave (Cartagena, SE Spain). We suggest that physical weathering of carbonate host-rock was driven by precipitation of soluble sea-salts (mostly gypsum and halite), and this process controlled the recent geomorphological evolution of the cave. The Triassic carbonate host-rock shows clear evidence for salt weathering, including gypsum/halite infillings in

33 cracks of the bedrock, mechanical spalling of the carbonate, and detachment of

34 rock fragments that lead to the formation cave voids and in-situ accumulations of

35 piles of unsorted rubble. Sulfur and oxygen isotopes of gypsum sulfate

36 ($3.0‰ < \delta^{18}O < 11.6‰$ and $16.7‰ < \delta^{34}S < 20.7‰$) are generally lower than modern

37 seawater sulfate and suggest contributions from a ^{34}S-depleted source (i.e.

38 oxidation of pyrite). The $\delta^{18}O$ and δD of gypsum hydration water are relatively low

39 compared to expected values for the evaporation of pure seawater to gypsum

40 saturation, suggesting that gypsum precipitation involved a secondary calcium-

41 sulfate source or recycling of gypsum from previous stages, along with mixing of

42 seawater and meteoric water seepage to the cave. The $^{87}Sr/^{86}Sr$ in gypsum

43 shows intermediate values between modern seawater and Triassic carbonate

44 values because of interaction between the solution and the bedrock. The

45 salinities of the speleothem-forming solutions are relatively high (13.2 ± 3.2 wt. %

46 eq. NaCl) compared to gypsum formed from evaporated brackish solutions (i.e.

47 ~4-8 wt. % eq. NaCl) and indicate dissolution of earlier evaporites before

48 secondary gypsum precipitation. This cave-forming mechanism, which is related

49 to saline water circulation and precipitation of evaporitic minerals, may be

50 common in other coastal caves.

51

52 **KEYWORDS:** coastal caves, evaporites, gypsum, halite, salt weathering,

53 gypsum speleothems, stable isotopes.

1. Introduction

The mechanisms involved in the formation of caves (i.e. speleogenesis) are generally linked to dissolution of carbonate host-rock by freshwaters undersaturated in calcium carbonate (see Audra and Palmer, 2015 for a recent review). These karstification processes create voids in the rock that can result in the breakdown and collapse of cave ceilings, eventually leading to the formation of large chambers and passages (Ginés and Ginés, 2007).

In the case of coastal caves, the dissolution of the carbonate host-rock can be enhanced by the mixing of freshwater and seawater that generates solutions undersaturated in calcite ($CaCO_3$) and dolomite ($CaMg(CO_3)_2$). These undersaturated solutions are capable of dissolving limestone and dolostones, accelerating cave forming processes (Mylroie and Mylroie, 2007). In addition to karstification processes, speleogenesis in coastal caves can be driven by the geomorphological evolution of the shoreline, in many cases connected to coastal erosion that causes landslides and fracturing (Moore, 1954). Caves that develop in coastal fractures (e.g. 'flank margin caves') display distinctive features compared to caves formed by dissolution (Mylroie and Carew 1990) and lack specific features generated by a subterranean water course or phreatic conduits, such as 'scallops' and smoothed surfaces (Mylroie and Mylroie, 2007). Additional geochemical processes in coastal karstic aquifers can also result in the formation of subterranean voids; potential mechanisms include mechanical weathering caused by the pressure generated in pores of the carbonate host-rock because of the precipitation of soluble salts (i.e. 'gypsum/halite wedging'; White and White,

78   2003). However, the relative importance of salt weathering processes in coastal

79   cave environments remains uninvestigated.

80

81   Salt weathering is known to influence the development of many geomorphologic

82   features in different environments, including honeycombs and alveoles (Mustoe,

83   1982), tafoni, and cave genesis in granitic rocks (Bradley et al., 1978).

84   Furthermore, this mechanism is an important contributor to rock debris generation

85   in arid regions (Beaumont, 1968; Goudie and Day, 1980), coastal environments

86   (Mottershead, 1989), and cold settings (Prebble, 1967). In this study, we examine

87   the mineralogy and geochemistry of secondary evaporite deposits in El Orón-

88   Arco Cave of Cabo Tiñoso ('Scabby Cape', Cartagena, Region of Murcia, SE

89   Spain) in order to evaluate the role of sea salt weathering during its formation.

90   Oxygen and sulfur isotopes of sulfate in gypsum ($CaSO_4 \cdot 2H_2O$) are utilized to

91   determine the sources of sulfate for the formation of the gypsum speleothems.

92   Oxygen and hydrogen isotopes in structurally-bonded gypsum hydration water

93   (GHW) and salinity of fluid inclusions (i.e. microthermometry of fluid inclusions)

94   are used to identify the source of water (seawater vs meteoric seepage; e.g.

95   Evans et al., 2015), the degree of evaporation of the solution in the cave, and

96   potential recycling of older evaporites before the precipitation of the gypsum

97   speleothems. Strontium isotopes in gypsum and soluble salts in pores of the host-

98   rock are used as an indicator of the degree of contribution of cations (calcium and

99   strontium) from the cave matrix to the solution before gypsum precipitation. We

100 generate a model to explain the cave formation based on geomorphological and

101 geochemical observations, with potential implications for the genesis of other

102 coastal caves.

2. Geological setting and cave description

El Orón-Arco Cave system is located in the southern flank of Cabo Tiñoso in Cartagena, Murcia Region, SE Spain (Fig. 1). The cavity consists of a subterranean network that extends over 1500 m, from El Arco Cave in the south-east, first surveyed in the 1980s (Llamusí et al., 1990), to the more recently discovered El Orón Cave in the north-west (Puch, 1998). El Arco Cave is also known as the 'Cave of the Great Lake' because of the presence of a 1200 m^2 brackish lake with a maximum depth of 2 m. The largest cave chamber is the 'Hall of the Chandeliers', which is located between 40 and 170 m a.s.l., representing the highest point in the cave above sea level. The rest of the passages and chambers lie between the sea level and ~40 m a.s.l. There are two entrance locations to El Orón-Arco Cave; the first is via a submarine access point (2 m b.s.l.), whereas the second consists of a subaerial entrance in the cliff of Cabo Tiñoso (~10 m a.s.l.) (Fig. 1).

The cave has formed along a fracture running NW to SE, parallel to the shoreline, in the highly foliated Triassic limestone and dolostone of the Alpujarride Formation of Cabo Tiñoso (García-Tortosa et al., 2000). A series of greyish limestones and interbedded reddish dolostones outcrop both in the cave (Fig. 2A) and outside (Fig. 2B). No evidence for phreatic dissolution or signs of subterranean runoff are found in the cave, whereas two brackish-water lakes at sea-level are the only known waterbodies at present.

127 Climate in this region is semi-arid, with mean annual temperature around 20 °C,

128 maximum temperatures in August (~28 °C) and minimum in January (~14 °C).

129 Average annual precipitation rarely exceeds 250 mm in this region and is one of

130 the driest areas of the Iberian Peninsula. Vegetation over the cave consists of

131 thermo-Mediterranean pre-desertic scrubs and xerophilic herbs.

132

133 **3. Methods**

134 **3.1. Sampling of speleothems**

135 We performed a detailed photographic study of the geomorphological and

136 speleothemic features of El Orón-Arco Cave (Figs. 2 and 3) and collected 27

137 mineral samples for mineralogical and stable isotopes analyses (Fig. 1 for

138 sampling site locations; Figs. 2 and 3 and Table 1 for sample descriptions). In

139 general, sample amounts were smaller than 5 g and were preferentially selected

140 from discreet parts of the chambers to minimize the impact on the cave

141 environment.

142

143 Saline concretions on the cave walls were sampled from foliation planes of the

144 host-rock in different sectors of the cave (n=8) (Figs. 2A and 3). We took samples

145 of the foliated greyish and reddish materials that comprise the host-rock inside

146 and outside the cave (n=4) (Fig. 2B), and one sample of yellowish calcschists

147 from outside of the cave entrance. A sample of yellowish unconsolidated, sandy

148 material was taken from a fracture following the foliation of the greyish host-rock

149 in the Hall of the Chandeliers. In the same chamber, a sample of the whitish

150 microcrystalline crust that occurs all over the ceiling in this location was collected

151 (Fig. 3E). Another sample comprises a ~5 cm fragment from a ~1 m long

152 transparent euhedral crystal that hangs from the cave ceiling, resembling a

153 'chandelier' (Fig. 3E), and morphologically similar to those described in

154 Lechuguilla Cave, New Mexico, USA (Davis, 2000). In places, the apices of these

155 crystals display a ~10 cm long and 1 cm wide hollow cylinder, resembling a soda-

156 straw, made of a transparent microcrystalline mineral (Fig. 3F). In the 'Hall of the

157 Eccentrics', we took a ~5 g fragment of a hollow gypsum hemisphere, ~20 cm in

158 diameter from the cave ceiling (called 'blisters' hereafter), which are surrounded

159 by (but generally not in contact with) carbonate speleothems (Fig. 3H). Similar

160 'blister' speleothems have been described in Cupp-Coutunn Cave, Turkmenistan

161 (Maltsev and Self, 1992). Lastly, a transparent single crystal was collected from

162 the tip of a stalactite (Fig 3I). Samples (~250 mg) were ground to a fine powder

163 and dried at 45 °C overnight for mineralogical and isotopic analyses.

164

165 **3.2. Mineralogical analyses**

166 A transmission X-ray diffraction (XRD) instrument (Terra), inXitu, Inc. (California),

167 was utilized to determine the mineralogy of 27 samples (Sarrazin et al., 2005) at

168 the Unidad Asociada al Centro de Astrobiologia CAB-CSIC-UVa of Valladolid

169 University (Valladolid, Spain). Powdered samples were initially transferred into a

170 vibrating cell. A micro-focused X-ray source (Co) (10 W) was combined with

171 miniature slits to produce a low divergence beam illuminating the sample at a 10°

172 incidence angle. A custom CCD camera (Andor™) was used to collect the XRD

173 signal over a range of 5-55° of 2θ. X-ray diffractogram resolution was 0.3° of the

174 2θ angle. Sections of diffraction rings were collected in 2D images, while the 1D

175 XRD patterns were calculated by circumferential integration of the diffracted

176 intensities along diffraction rings. Diffractograms were processed by the X-

177 Powder software (Martín, 2004) and mineralogical determination used the PDF-

178 2 (Power Diffraction Files) database.

179

180 **3.3. Stable isotope analyses**

181 **3.3.1. Sulfur (δ^{34}S) and oxygen ($\delta^{18}O_{SO4}$) in sulfate**

182 The sulfur and oxygen isotopes of the sulfate of 13 samples were analyzed in the

183 Godwin Laboratory at the University of Cambridge (UK). Powdered gypsum

184 samples (~5 mg) were dissolved in deionized water at 45 °C overnight. The

185 effluent containing the aqueous sulfate from the dissolution was then separated,

186 and a barium chloride solution (50 g/L) was added to induce $BaSO_4$ precipitation.

187 The $BaSO_4$ was rinsed with 6 M HCl to remove carbonates, and subsequently

188 rinsed 3 times with deionized water. The samples were then dried at 45 °C

189 overnight.

190

191 For $\delta^{18}O_{SO4}$, a High Temperature Conversion Element Analyzer (TC/EA) was

192 used to pyrolyze the $BaSO_4$ at 1450 °C and produce CO, which was measured

193 by continuous flow Gas Source Isotope Ratio Mass Spectrometry

194 (ThermoScientific Delta V Plus). All $\delta^{18}O_{SO4}$ are reported relative to V-SMOW

195 (Vienna-Standard Mean Ocean Water). Samples were run in triplicate, alongside

196 the NBS-127 Standard (8.6‰), and the standard deviation of the replicate

197 analyses was better than 0.5‰ (1σ).

198

199 For $\delta^{34}S_{SO4}$, the $BaSO_4$ was combusted at 1030°C in a Flash Elemental Analyzer

200 (Flash-EA), and the sulfur dioxide produced was measured by continuous flow

201 Gas Source Isotope Ratio Mass Spectrometry (ThermoScientific, Delta V Plus).

202 All $\delta^{34}S_{SO4}$ are reported relative to VCDT (Vienna-Canyon Diablo Troilite).

203 Samples for sulfur isotope analysis were run in duplicate, alongside the NBS-127

204 standard (20.3‰). The reproducibility (1σ) of $\delta^{34}S_{SO4}$ of the duplicate analyses

205 was better than 0.2‰, similar to the long-term reproducibility of the NBS-127 over

206 the run (0.2‰).

207

3.3.2. $\delta^{18}O$ and δD of gypsum hydration water (GHW)

209 The GHW of 8 samples was extracted by slowly heating each sample (~200 mg)

210 to 400 °C, *in vacuo,* using a bespoke offline extraction system consisting of six

211 vacuum lines contained within a modified gas chromatography (GC) oven,

212 following the method of Gázquez et al. (2015a). Oxygen ($\delta^{18}O$) and hydrogen

213 (δD) isotopes in GHW were measured simultaneously by cavity ring down

214 spectroscopy (CRDS) in the Godwin Laboratory at the University of Cambridge

215 (UK) using a L1102-i Picarro water isotope analyzer (Hodell et al., 2012; Evans

216 et al., 2015; Chen et al., 2016). All results are reported in parts per thousand (‰)

217 relative to V-SMOW. Calibration of results to V-SMOW was achieved by

218 analyzing internal standards before and after each set of 10 or 12 samples.

219 Internal standards were previously calibrated against V-SMOW, GISP, and

220 SLAP. External error (1σ) of the method was ±0.1‰ for $\delta^{18}O$ and ±0.6‰ for δD,

221 as estimated by repeated analysis (n=3) of an analytical grade standard,

222 extracted together with the samples in each run of the extraction apparatus

223 (Gázquez et al., 2015a).

224

3.3.3. Strontium isotopes

226 Strontium isotope ($^{87}Sr/^{86}Sr$) measurements were made by thermal ionization

227 mass spectrometry (Thermo-Scientific Triton Plus MC-TIMS) at the University of

228 Cambridge. Approximately 2.5 mg of powdered gypsum (n=3) was processed for

229 isotopic analysis. Gypsum was ground to a fine powder and dissolved in

230 deionized water. Carbonate samples were also ground placed in deionized water

231 for 24 h to extract soluble salts. The supernatant fluid was stored for isotopic

232 analysis (n=2). The carbonate samples themselves (n=2) were prepared for

233 isotope analysis by treating the samples with methanol, 10% ammonium

234 hydroxide and water washes (to mechanically remove clays and adsorbed ions),

235 each step performed in triplicate. To isolate the carbonate phase, the solid

236 sample was dried, weighed and placed in a volume of 0.1M HCl containing 110%

237 of the acid required for complete dissolution of the carbonate, calculated to avoid

238 elemental variation generated by incomplete dissolution.

239

240 An aliquot of each sample solution containing approximately 300 ng of strontium

241 was dried down, dissolved in 200 µl 3M HNO_3 and refluxed at 80 °C for 3 hours.

242 Strontium was separated using Eichrom Sr Spec resin with 100 µm to 150 µm

243 mesh particle size in clean lab conditions. The separated Sr was dried down,

244 refluxed in 3N HNO_3 and subsequently dried down once again. Samples were

245 then loaded onto degassed single Re filaments together with 1 µl of tantalum

246 phosphate activator. A current of ~0.8A was continuously applied during the

247 loading. The evaporation filament is heated manually until a stable signal

248 between 4V and 6 V of ^{88}Sr on a $10^{11}\Omega$ resistor was reached. Data acquisition

249 was comprised of 10 blocks of 20 measurements with a ~8 s integration time in

250 static mode. Results were normalized to $^{88}Sr/^{86}Sr$ 0.1194 with an exponential

251 fractionation correction. Runs were bracketed with the NBS 987 standard. Eleven

252 analyses of NBS 987 during 2 months before and after this study gave a mean

253 value of 0.710253 (2σ = 0.000007). Blanks were <250 pg and negligible for the

254 Sr concentration of these samples.

255

256 **3.4. Microthermometry of fluid inclusions**

257 The method for microthermometric analysis of fluid inclusions in gypsum closely

258 followed that described by Attia et al. (1995) and Evans et al. (2015). Thin (<1mm)

259 sections of gypsum were obtained by cleaving the mineral along 010 planes using

260 a razor blade. The fragments were placed in a Linkam THMSG600 heating-

261 freezing stage attached to a Zeiss Axio Scope.A1 microscope. The ice melt

262 temperature (T_m) of primary fluid inclusions (identified as described in Attia et al.

263 1995) in samples CT-15B (n=11), CT-21B (n=10) and CT-23 (n=4) was

264 determined following the procedure described by Evans et al. (2015). T_m was

265 recorded to within 0.1 °C and reproduced at least twice for each inclusion with an

266 error of ±0.2 °C. Salinities of the fluid inclusions were calculated from the final T_m

267 and expressed as weight % NaCl equivalent (Bodnar, 1993).

268

269 **4. Results**

270 **4.1. Mineralogy**

271 The cave host-rock comprises an alternate sequence of limestone (grey

272 materials) and dolostone (reddish materials) beds that outcrop inside and outside

273 the cave (Fig. 2 A and B). Most of the concretions, infillings and coatings in the

274 Passage of the Debris and the Hall of the Chandeliers are made of

275 microcrystalline gypsum (Fig. 3C) and halite (NaCl) (Fig. 3G), with minor dolomite

276   and celestine ($SrSO_4$) and occasionally brownish sugary-textured calcite (Fig.

277   3D). The mineralogical analyses confirm that the microcrystalline coatings in the

278   ceiling of the Hall of the Chandeliers and in the selenite crystals of the

279   'chandeliers' (Fig. 3E) are made of high-purity gypsum. The apices of some of

280   the chandeliers are made of a halite cylinder, containing traces of celestine (Fig.

281   3F). The 'boxwork' structures of the 'Hall of the Boxwork' is composed of dolomite

282   blades (with minor calcite), covered by gypsum coatings (Fig. 3G). In the Hall of

283   the Eccentrics, the 'blister' speleothems are made of gypsum, while the inner

284   stalactites are composed of aragonite (Fig. 3I). All the analyzed stalactites in this

285   chamber are composed of aragonite, which in places display single gypsum

286   crystals hanging from their tips (Fig. 3J).

287

288   **4.2. Stable isotopes**

289   **4.2.1 Sulfur and oxygen in sulfate**

290   The $\delta^{34}S$ values in gypsum speleothems range from 16.7‰ to 20.7‰, and the

291    $\delta^{18}O_{SO4}$ in sulfate ranges from 3.0‰ to 11.6‰. The $\delta^{34}S$ and $\delta^{18}O_{SO4}$ show a

292   positive correlation with slope of 1.3 (Fig. 4). The gypsum coatings from the

293   Passage of the Boxwork display higher $\delta^{34}S$ and $\delta^{18}O_{SO4}$, within the range of

294   modern marine sulfate (~20‰ and ~9‰, respectively). The rest of samples fall

295   out of this range and generally have lower $\delta^{34}S$ and $\delta^{18}O_{SO4}$ values.

296

297   **4.2.2 $\delta^{18}O$ and δD of gypsum hydration water**

298   The $\delta^{18}O$ and δD in GHW of speleothems from El Orón-Arco Cave range from

299   2.0‰ to 5.8‰ and from -24.8‰ to -13.6‰, respectively. The oxygen and

300   hydrogen isotope composition of the parent water from which the gypsum formed

301   is calculated by using the values of GHW and known fractionation factors

302   ($\alpha^{18}O_{gypsum-water}$ and $\alpha D_{gypsum-water}$), which are practically insensitive to temperature

303   between 5 °C and 30 °C (Gázquez et al., 2017a; Liu et al., 2018). The $\alpha D_{gypsum-water}$

304   is relatively sensitive to water salinity (3×10^{-5} per g/L of NaCl between 30 g/L

305   and 300 g/L), whereas $\alpha^{18}O_{gypsum-water}$ is not affected by salinities less than 150

306   g/L of NaCl (Gázquez et al., 2017a). Gypsum samples in this study precipitated

307   mostly from solutions with salinities around 130-150 g/L (see section 4.3). We

308   use fractionation factors at 150 g/L ($\alpha^{18}O_{gypsum-water}$ of 1.0033 and $\alpha D_{gypsum-water}$ of

309   0.985; Gázquez et al, 2017a). Changes in temperature of ±5°C, result in

310   uncertainty of ±0.5‰ in the calculated values of δD of the mother water, which is

311   insignificant given the analytical precision of the measurements (±0.6‰).

312   Changes in salinity of ±50 g/L would result in uncertainties of ±1.5‰ in δD of the

313   mother water, which is also irrelevant for our application.

314

315   By applying the selected isotope fractionation factors to the isotope composition

316   of GHW, we found that the $\delta^{18}O$ of the speleothem-forming water ranges from -

317   0.7‰ to 2.5‰, while δD ranges from -9.9‰ to 3.2‰. The speleothems from the

318   Hall of the Eccentrics show the lower $\delta^{18}O$ and δD values, whereas gypsum in

319   the Hall of the Chandeliers precipitated from a solution more enriched in the

320   heavy isotopes (Table 1 and Fig. 5). Together, the $\delta^{18}O$ and δD of the

321   speleothem-forming water values describe a line with a slope of ~3.3.

322

323   4.2.3. Strontium isotopes

324   The $^{87}Sr/^{86}Sr$ of the analyzed gypsum speleothems is 0.70815±0.00005 (n=3).

325   The lowest value corresponds to the gypsum 'blisters' from the Hall of the

326   Eccentrics (0.708095), while the highest $^{87}Sr/^{86}Sr$ value is found in the gypsum

327   coatings from the Passage of the Debris (0.708188). The carbonate host-rock

328   shows consistently lower $^{87}Sr/^{86}Sr$ values of 0.70779 ± 0.00007 (n=2). The

329    $^{87}Sr/^{86}Sr$ of the water-soluble salt leaches from the host-rock display intermediate

330    $^{87}Sr/^{86}Sr$ values between the gypsum speleothems and the host-rock of

331   0.70796 ± 0.00004 (n=2) (Fig. 6).

332

333   **4.3. Fluid inclusions**

334   The ice melt temperatures (T_m) of primary fluid inclusions in gypsum speleothems

335   range from -15.7 °C to -3.3 °C (n=27), corresponding to salinities from 19.2 to 5.4

336   wt. % eq. NaCl. The gypsum 'chandeliers' (Fig. 3E) have the lowest T_m (-

337   10.7 ± 2.5°C; n=12) and therefore, the highest salinity of fluid inclusions (14.2 ± 2.5

338   wt. % eq. NaCl), while the gypsum spar on the tip of an aragonite stalactite (CT-

339   23A1) from the Hall of the Eccentrics displays the highest T_m (-5.5$\pm$1.9°C; n=4)

340   and lowest salinities (8.2 ± 2.5 wt. % eq. NaCl). Another gypsum spar (CT-21A;

341   Fig. 3J) from the same chamber shows intermediate T_m values (-9.9$\pm$2.4°C; n=11)

342   and salinities (13.7 ± 2.4 wt. % eq. NaCl). Altogether, the mean T_m is -9.5$\pm$2.9°C

343   and the salinity is 13.2 ± 3.2 wt. % eq. NaCl, on average (Fig. 7).

5. Discussion

5.1. Geomorphological and mineralogical evidence for sea salt weathering

There is no physical evidence of either phreatic or vadose dissolution that would support conventional karstification mechanisms operating in the El Orón-Arco Cave today. As in many other 'flank margin coastal caves', El Orón-Arco Cave lacks both the typical morphologies related to water flow and indicators of subaqueous carbonate dissolution (e.g. scallops, smoothed surfaces or cupolas, etc.) (Mylroie and Mylroie, 2007). In contrast, the cavity displays clear evidence of recent mechanical weathering processes (Fig. 8). It should be noted that, while there is no evidence for conventional speleogenesis within El Orón-Arco Cave, it cannot be ruled out that the initial stages of the cave speleogenesis were controlled by phreatic or vadose dissolution processes. This may have led to the enlargement of the subterranean network before the stage of physical weathering. The signs of such hypothetical dissolution mechanisms might have been masked by the subsequent effects of subaerial sea salt weathering. In addition, the motion of faults system that runs parallel to the cliff of the Cabo Tiñoso may have played a main role in the initial stages of the cave formation by creating preferential groundwater pathways that favored the karstification of the carbonate host-rock.

The unsorted carbonate host-rock fragments (<1 mm to tens of centimeters) that rest against the walls of the 'Passage of the Debris' and in the entrance of the 'Passage of the Boxwork' provide strong evidence of a mechanical cave-forming mechanism that has operated in the cave at least in recent times (Fig. 2D). The cave walls and ceilings are made of easily detachable rock that crack and

369   eventually fall naturally to the cave floor, accumulating as piles of unsorted rubble.

370   This process is currently active and was observed during our visits to the cave.

371   Indeed, the accumulation of rock debris in the smaller passages (e.g. the access

372   to the Passage of the Boxwork) represents a serious challenge when accessing

373   the cave, since these galleries are prone to obstruction and frequently need to be

374   unblocked by speleologists.

375

376   Mineralogical analyses of cave wall materials reveal the presence of minerals

377   typically derived from evaporated seawater, including halite, gypsum and

378   occasionally calcite (Table 1). The cave host-rock is predominantly composed of

379   greyish limestone and reddish dolostone, the latter containing small amounts of

380   iron oxides. In the planes of the carbonate beds, whitish and yellowish saline

381   concretions and efflorescences are observed projecting out into the cave (Figs.

382   2C and 3C). A mechanism is needed to explain the presence of evaporitic

383   minerals within the host-hock material and the formation of weathered debris on

384   the cave floor.

385

386   We suggest that capillary action and infiltration of seawater through the carbonate

387   formation of Cabo Tiñoso followed by evaporation of the solution in the cave

388   results in the crystallization of evaporites in planes and pores, leading to

389   'gypsum/halite wedging' of the host-rock (Fig. 8). In the cave environment,

390   evaporation of infiltrated seawater is favored by the relatively high air temperature

391   in the cave (~19 °C during our visit in January 2012) and likely low relative

392   humidity. Although relative humidity has not been measured in the cave, the

393   presence of halite strongly indicates relatively dry conditions because halite

394 dissolves if atmospheric relative humidity is above ~73% (Wexler and Hasegawa,

395 1954; Oerter et al., 2018).

396

397 The crystallization pressure generated by the formation of salts in pore spaces

398 (e.g. Goudier and Viles, 1997; Rodriguez-Navarro and Doehne, 1999) caused

399 fracking and disaggregation of the original Triassic dolostones and limestones.

400 Moreover, the motion of the faults in the Cabo Tiñoso formation and eustatic sea-

401 level changes may have played a role in the ejection of the disaggregated

402 materials (Fig. 8). During periods of relatively high sea-level, parts of the cave

403 passage (today mostly between 0 and 50 m a.s.l.) were likely submerged in a

404 brackish aquifer. In this scenario, calcium ions could be released to the solution

405 from the limestones and dolostones and, in combination with the SO_4^{2-} from

406 seawater, result in the oversaturation of the solution for gypsum ($SI_{gyp}>0$) and

407 subsequent mineral precipitation in cracks and pores of the carbonate host-rock

408 (see section 5.3) (Fig. 8A). During periods of relatively low sea-level, these

409 primary evaporites would dissolve because of circulation of meteoric/brackish

410 water mixture undersaturated in gypsum and halite (Fig. 8B). The solution

411 enriched in dissolved salts could evaporate in the voids of the rock and the

412 crystallization pressure generated by the secondary minerals would result in a

413 significant sea salt weathering mechanism, as shown in Fig. 8.

414

415 The 'gypsum/halite wedging' process described above is a relatively uncommon

416 mechanism in caves and has only been described in a few subterranean sites,

417 including the Mammoth cave system in Kentucky, USA (White and White, 2003),

418 the Friars Hole cave system in West Virginia, USA (Jameson, 1991), and some

419 caves of the Nullarbor Plain, Australia (Lowry and Jennings 1974). Also, it is well

420 documented that similar processes of capillary action of saline waters and

421 crystallization of salts are responsible for the decay of building materials and

422 limestone sculptures (e.g. Cardell et al., 2008; Gómez-Laserna et al. 2013;

423 Gázquez et al., 2015b) and contribute to the formation of geomorphological

424 features, such as honeycombs, alveoles and tafoni, especially in dry regions

425 (Prebble, 1967; Beaumont, 1968; Bradley et al., 1978; Goudie and Day, 1980;

426 Mustoe, 1982; Mottershead, 1989). We use stable isotopes to test the sea salt

427 weathering hypothesis in sections 5.2 and 5.3.

428

429 **5.2. Identification of sulfate sources**

430 The $\delta^{18}O_{SO4}$ and $\delta^{34}S$ of secondary gypsum deposits in El Orón-Arco Cave are

431 generally lower than those expected for gypsum formed solely from modern

432 seawater ($\delta^{18}O_{SO4}$ ~9‰ and $\delta^{34}S$ ~21‰) (Fig. 4). The only samples that show

433 seawater-like sulfate isotopic composition are the gypsum crusts on the dolomite

434 boxwork formations found in the Passage of the Boxwork. In a $\delta^{18}O_{SO4}$-$\delta^{34}S$ plot,

435 the gypsum samples are positively correlated (slope of 1.3) and have $\delta^{18}O_{SO4}$ and

436 $\delta^{34}S$ down to 3‰ and 16.5‰, respectively.

437

438 During crystallization from the solution, gypsum precipitates with a negligible

439 sulfur isotope fractionation (Raab and Spiro, 1991; Van Driessche et al., 2016),

440 but as much as a 3‰ offset for oxygen isotopes, although the latter isotopic

441 fractionation factor is poorly constrained (Van Driessche et al., 2016). If the

442 sulfate that formed the gypsum was derived directly from seawater, the $\delta^{18}O_{SO4}$

443 and $\delta^{34}S$ of the gypsum should reflect seawater values. Subsequent solution-

444   reprecipitation of the gypsum in water with a similar $\delta^{18}O_{SO4}$ and $\delta^{34}S$ should not

445   alter the $\delta^{18}O_{SO4}$ and $\delta^{34}S$ of the gypsum significantly (Evans et al., 2015). Our

446   observations in El Orón-Arco Cave show that gypsum speleothems have

447   significantly lower oxygen and sulfur isotope values than modern marine sulfate,

448   so direct gypsum precipitation from seawater cannot completely explain our

449   observations.

450

451   The lower $\delta^{18}O_{SO4}$ and $\delta^{34}S$ may be derived from either (i) oxidation of isotopically

452   ^{34}S-depleted sulfur in sulfide minerals (e.g. pyrite) hosted in the carbonate

453   bedrock (e.g. Audra et al., 2015) or (ii) the oxidation of aqueous sulfide previously

454   reduced from marine sulfate by bacteria. Both sulfide minerals and aqueous

455   sulfide take at least one of their oxygen atoms from water upon oxidation,

456   producing sulfate that is more depleted in both the ^{34}S and ^{18}O isotopes.

457   No sulfide mineralization has been identified in the cave or in our samples by

458   mineralogical analyses. However, this region, including the nearby Sierras of

459   Cartagena and Mazarrón (~20 km from El Orón-Arco Cave), hosts important Zn-

460   Pb-Cu-Ag-Fe sulfide deposits that are related to volcanism and epigene

461   hydrothermal activity (Esteban-Arispe et al., 2016). Most regional sulfide minerals

462   have $\delta^{34}S$ values ranging from +2‰ to +15‰, and thus represent a potential

463   source of ^{34}S-depleted sulfates to the cave system compared to marine sulfate

464   (Table 1). We suggest that migration of fluids from depth through the faults

465   system of Cabo Tiñoso can explain the $\delta^{18}O_{SO4}$ and $\delta^{34}S$ values. This mechanism

466   assumes oxidation of ^{34}S-depleted sulfide to sulfate occurred in deeper strata,

467   followed by mobilization to the cave level and mixing with marine sulfate. Indeed,

468   in other caves affected by 'gypsum wedging' (e.g. Mammoth cave system,

469   Kentucky, US), the δ^{34}S values in gypsum (-12‰ to +12‰) have been interpreted

470   as being completely derived from oxidation of pyrite (Metzger et al., 2015). Thus,

471   we suggest that, although oxidation of sulfide minerals is not the primary source

472   of sulfate for gypsum precipitation in the El Orón-Arco Cave, mixing with marine

473   sulfate can explain the observed δ^{34}S values. As for $\delta^{18}O_{SO4}$, the relatively low

474     $\delta^{18}O_{SO4}$ observed in El Orón-Arco Cave can also be explained by oxidation of

475   sulfide, which incorporates oxygen atoms from meteoric water that is typically

476   depleted in the ^{18}O isotope (Van Stempvoort and Krouse, 1994; Onac et al.,

477   2011).

478   Alternatively, mixing of aqueous sulfate derived from the oxidation of sulfide

479   (previously reduced from seawater sulfate by bacteria) and marine sulfates may

480   explain the relatively low δ^{34}S and $\delta^{18}O_{SO4}$ in the gypsum speleothems in this

481   cave. Microbial sulfate reduction produces ^{34}S-depleted sulfides, with maximum

482   observed depletions of -72‰ (Sim et al., 2011), whereas the oxidation of sulfide

483   to elemental sulfur has a far lower sulfur isotope fractionation, producing

484   enrichments in the ^{34}S isotope on the order of +8‰ (Zerkle et al., 2016). Complete

485   oxidation of elemental sulfur to sulfate does not produce significant sulfur isotope

486   fractionation (Zerkle et al., 2016 and references therein). Bacterial sulfur

487   reduction and re-oxidation results in sulfates with low δ^{34}S and $\delta^{18}O_{SO4}$ values.

488   However, this mechanism requires anoxic conditions that may have never

489   occurred in El Orón-Arco Cave, where the presence of organic matter is scarce,

490   and oxygen concentration may have not been a limiting factor. In summary, the

491     $\delta^{18}O_{SO4}$ and δ^{34}S observed in El Orón-Arco Cave can be explained by mixing of

492   seawater sulfate and isotopically lower sulfate derived from oxidation of sulfide

493   minerals in depth and transported to the cave level though the faults system.

494

495   **5.3. Modes of gypsum/halite precipitation**

496   Gypsum precipitation has been identified as the cause of aqueous sulfate

497   depletion in the fronts of marine water intrusions in coastal aquifers (Gomis-

498   Yagües et, 2000; Boluda-Botella et al., 2004). The meteoric-seawater mixture in

499   the mixing zone of coastal aquifers is generally undersaturated in gypsum

500   ($SI_{gyp}<0$). However, the intrusion front contains relatively high concentrations of

501   dissolved ions (mostly SO_4^{2-}, Cl^-, Ca^{2+}, Mg^{2+} and Na^+) that can interact with the

502   carbonate bedrock. Magnesium and sodium can displace calcium in limestones

503   and dolostones, resulting in an increase of calcium in the solution that, together

504   with high sulfate concentrations in seawater, can lead to $SI_{gyp}>0$ and gypsum

505   precipitation (Gomis-Yagües et, 2000; Boluda-Botella et al., 2004).

506

507   Strontium isotope ratios provide a tracer between marine-sourced fluids and other

508   strontium-bearing fluids as each endmember is often characterized by different

509   strontium concentrations and $^{87}Sr/^{86}Sr$. Because of the long residence time of

510   strontium relative to the mixing time of the ocean, $^{87}Sr/^{86}Sr$ is homogeneous in

511   the global ocean. Strontium in modern seawater has a radiogenic $^{87}Sr/^{86}Sr$

512   (0.70916) which differs significantly from other sources of strontium such as fluids

513   produced from the weathering of silicate (>0.720) and carbonate (<0.708)

514   lithologies (Elderfield, 1986). The host-rock of El Orón-Arco Cave shows relatively

515   low $^{87}Sr/^{86}Sr$ values (0.70779±0.00007), that are similar to those expected for

516   Triassic marine carbonates (0.7078; McArthur et al., 2001). The $^{87}Sr/^{86}Sr$ of the

517 gypsum speleothems is 0.70815±0.00005 (n=3), thus displaying higher $^{87}Sr/^{86}Sr$

518 than those of the host-rock, but considerably lower $^{87}Sr/^{86}Sr$ than modern

519 seawater. The soluble-salts leaches from the host-rock have intermediate

520 $^{87}Sr/^{86}Sr$ between the Triassic carbonate and the speleothems (Fig. 6). This

521 suggests that strontium in the speleothem-forming solution comes primarily from

522 the Triassic carbonate (~75%) dissolution by brackish aquifer water before

523 gypsum precipitation, rather than from modern marine strontium (~25%). This

524 mechanism of host-rock dissolution was therefore also responsible for enhanced

525 calcium concentration in the solution that lead to $SI_{gyp}>0$ and gypsum precipitation

526 in cracks of the host-rock.

527

528 The gypsum precipitation process often requires evaporation of the fluid for the

529 solution to reach $SI_{gyp}>0$, as observed in other caves (Forti, 1996; Filippi et al.,

530 2011; Gázquez et al., 2005c; 2017b). In such situations, $\delta^{18}O$ and δD of the

531 evaporated water normally produce a line in $\delta^{18}O$ vs δD space with a slope less

532 than 8. However, by adding calcium and sulfate to the solution, gypsum can

533 precipitate directly from the solution with little evaporative enrichment. We test

534 both hypotheses by studying the stable isotopes of GHW. Because the $\delta^{18}O$ and

535 δD is recorded by the structurally-bound hydration water of evaporative gypsum,

536 evaporative processes (or lack therefor) can be constrained (Evans et al., 2015,

537 2018; Gázquez et al., 2017b; 2018).

538

539 The $\delta^{18}O$ and δD values of the speleothem-forming solution in El Orón-Arco Cave

540 do not fall in the field of non-evaporated seawater ($\delta^{18}O$ and $\delta D \sim 0$‰), nor do

541 they indicate gypsum precipitation from evaporated seawater to the point of

542 gypsum saturation (e.g. Evans et al., 2015; Gázquez et al., 2017a), which

543 displays much greater $\delta^{18}O$ and δD values than observed. Instead, the isotope

544 values of the speleothem-forming water fall on an evaporation line that probably

545 departed from an intermediate point between seawater values and the meteoric

546 water seepage ($\delta^{18}O$ of ~-5‰ and δD of ~-40‰ in SE Iberian Peninsula; e.g.

547 Gázquez et al., 2017b) (Fig. 5). This demonstrates that (1) the speleothem-

548 forming solution was a mixture of fresh-meteoric water and seawater and (2) that

549 this solution underwent significant evaporation in the cave before gypsum

550 precipitation.

551

552 Surprisingly, the salinity of the speleothem-forming waters (13.2±3.2 wt. % eq.

553 NaCl) was considerably higher than expected for gypsum formed from an

554 evaporated brackish solution (i.e. ~4-8 wt. % eq. NaCl; Attia et al., 1995;

555 Natalicchio et al., 2014; Evans et al., 2015) and more similar to the salinity of fluid

556 inclusions in purely evaporated seawater to gypsum saturation (i.e. ~12-14 wt. %

557 eq. NaCl). This apparent discrepancy between the results of stable isotopes in

558 GHW and salinity of fluid inclusions can be explained by a mechanism involving

559 (1) remobilization of halite/gypsum previously precipitated in cracks of the host-

560 rock that is easily dissolved by water undersaturated in halite and gypsum (e.g.

561 meteoric/seawater mixture); and (2) evaporation once the solution reaches the

562 cave, resulting in precipitation of gypsum with relatively high salinity of fluid

563 inclusions, but relatively low $\delta^{18}O$ and δD values (Fig. 8). Alternatively, partial

564 post-depositional isotopic exchange of GHW with an isotopically ^{18}O-depleted

565 source (i.e. meteoric waters) or gypsum reprecipitation, particularly in the case of

566 microcrystalline gypsum speleothems (e.g. Fig. 3I), could be argued (Sofer, 1978;

567   Pierre, 2018). However, this alteration may also derive secondary fluid inclusions

568   with lower salinities, which have not been observed in the analyzed samples from

569   El Orón-Arco Cave.

570

571   **6. Conclusions**

572   We demonstrate that the genesis of El Orón-Arco Cave was linked to the motion

573   of faults that runs parallel to the cliff of the Cabo Tiñoso, and to salt weathering

574   of the carbonate host-rock by infiltration and capillary action of seawater that

575   subsequently evaporates within the cave, leading to precipitation of evaporite

576   minerals (gypsum and halite) in pores and planes of the carbonate. The

577   crystallization pressure of salts produces cracking of the host-rock at different

578   scales. The detached rock fragments accumulate in piles that rest against the

579   cave walls. The same process of seawater infiltration is responsible for the

580   precipitation of gypsum and halite in speleothems of uncommon morphology,

581   including gypsum chandeliers, halite soda-straws and gypsum blisters.

582

583   The source of sulfates for gypsum precipitation is predominantly marine, although

584   the $\delta^{34}S$ and $\delta^{18}O_{SO4}$ results are lower than those expected during the formation

585   from modern seawater alone, suggesting a mixing of marine source fluids with an

586   isotopically depleted sulfate source (i.e. oxidation of sulfide minerals). The

587   isotopic composition of GHW and relatively high salinity of fluid inclusion in

588   gypsum crystals can be explained by recycling of evaporites (gypsum and halite)

589   from previous stages and gypsum reprecipitation in the form of speleothems. The

590   salt-weathering mechanism proposed here for the formation of El Orón-Arco

591   Cave is probably not an isolated case and may be responsible for the formation

592 of other caves elsewhere, both in coastal environments of dry regions and saline

593 settings (e.g. caves associated to saline diapirs).

594

605

606 **7. References**

607 Attia, O. E., Lowenstein, T.K., Wali, A.M.A. 1995. Middle Miocene gypsum, Gulf

608   of Suez: marine or nonmarine? J. Sediment. Res. 65A (4), 614–626.

609 Audra, Ph., Palmer A. 2015. Research frontiers in speleogenesis. Dominant

610   processes, hydrogeological conditions and resulting cave patterns. Acta

611   Carsolog. 44(3), 315-348.

612 Audra, Ph., Gázquez, F., Rull, F., Bigot, J.Y., Camus, H. 2015. Hypogene Sulfuric

613   Acid Speleogenesis and rare sulfate minerals in Baume Galinière Cave

614   (Alpes-de-Haute-Provence, France). Record of uplift, correlative cover

615   retreat and valley dissection. Geomorphology 247, 25-34.

616   Beaumont, P. 1968. Salt weathering on the margin of the Great Kavir, Iran. Geol.
617   Soc. Am. Bull. 79, 1683-1684.

618   Bodnar, R. 1993. Revised equation and table for determining the freezing point
619   de-pression of H2O–NaCl solutions. Geochim. Cosmochim. Acta 57 (3),
620   683–684.

621   Boluda-Botella, N., Gomis-Yagües, V., Ruiz-Beviá, F., Saquete-Ferrándiz, MD.
622   2004. Gypsum precipitation/dissolution during seawater intrusion. 18th Salt
623   Water Intrusion Meeting. Cartagena (Spain).

624   Bradley, W.C., Hutton, J.T., Twidale, C.R. 1978. Role of salts in development of
625   granitic tafoni, South Australia, J. Geol. 86, 647-654.

626   Cardell, C., Benavente, D., Rodriguez-Gordillo, J. 2008. Weathering of limestone
627   building material by mixed sulfate solutions. Characterization of stone
628   microstructure, reaction products and decay forms. Mate Charact, 59, 1371-
629   1385.

630   Chen, F., Turchyn A.V., Kampman N., Hodell D., Gazquez, F., Maskell, A. Bickle,
631   M.J. 2016. Isotopic analysis of sulfur cycling and gypsum vein formation in a
632   natural CO_2 reservoir. Chem. Geol. 436, 72-83.

633   Davis, D.G. 2000. Extraordinary features of Lechuguilla Cave, Guadalupe
634   Mountains. J. Cave Karst Stud. 62, 147-157.

635   Elderfield, H. 1986. Strontium isotope stratigraphy. Palaeogeogr. Palaeoclimatol,
636   Palaeoecolog. 57 (1), 71–90.

637   Esteban-Arispe, I., Velasco-Roldán, F., Boyce, A.J, Morales-Ruano, S., Yusta, I.,
638   Carrillo-Rosúa, J. 2016. Unconventional non-magmatic sulfur source for the
639   Mazarrón Zn-Pb-Cu-Ag-Fe epithermal deposit (SE Spain). Ore Geol. Rev., 72,
640   1102-1115.

641 Evans, N. P., Turchyn, A. V., Gázquez, F., Bontognali, T. R. R., Chapman, H. J.
642   and Hodell D. A. 2015. Coupled measurements of $\delta^{18}O$ and δD of hydration
643   water and salinity of fluid inclusions in gypsum from the Messinian Yesares
644   Member, Sorbas Basin (SE Spain). Earth Planet. Sci. Lett. 430, 499–510.

645 Evans, N.P., Bauska, T.K., Gázquez, F., Brenner, M., Curtis, J. H., Hodell, D. A.
646   2018. Quantification of drought during the collapse of the classic Maya
647   civilization. Science, 361 (6401), 498–501.

648 Filippi, M., Bruthans J., Palatinus L., Zare M. and Asadi N. 2011. Secondary halite
649   deposits in the Iranian salt karst: general description and origin. Int. J. Speleol,
650   40 (2), 141-162.

651 Forti, P. 1996. Speleothems and cave minerals in gypsum caves. Int. J. Speleol.
652   25, 91–104.

653 García-Tortosa, F.J., López-Garrido, A., Sanz de Galdeano, C. 2000. Las
654   unidades de Cabo Tiñoso y Peñas Blancas: Revisión y caracterización
655   estratigráfica de las unidades alpujárrides del sector entre Mazarrón y
656   Cartagena (Murcia, España). Estud. Geol.-Madrid, 56, 31-40.

657 Gázquez, F., Mather, I., Rolfe, J., Evans, N.P., Herwartz D., Staubwasser M.,
658   Hodell D.A. 2015a. Simultaneous analysis of $^{17}O/^{16}O$, $^{18}O/^{16}O$ and $^{2}H/^{1}H$ of
659   gypsum hydration water by cavity ring-down laser spectroscopy. Rapid
660   Commun. Mass Spectrom. 29, 1997–2006.

661 Gázquez, F., Calaforra, J. M., Forti, P., DeWaele, J., Sanna, L. 2015b. The role
662   of condensation in the evolution of dissolutional forms in gypsum caves: study
663   case in the karst of Sorbas (SE Spain). Geomorphology 229, 100–111.

Gázquez, F., Rull, F., Medina, J., Sanz-Arranz, A., Sanz, C. 2015c. Linking groundwater pollution to the decay of 15th-century sculptures in Burgos Cathedral (northern Spain). Environ. Sci. Pollut. Res. 22, 15677–15689.

Gázquez F., Evans N.P. and Hodell D.A. 2017a. Precise and accurate isotope fractionation factors ($\alpha^{17}O$, $\alpha^{18}O$ and αD) for water and $CaSO_4 \cdot 2H_2O$ (gypsum). Geochim. Cosmochim. Acta 198, 259–270.

Gázquez F., Calaforra J.M., Evans N.P. and Hodell D.A. 2017b. Using stable isotopes ($\delta^{17}O$, $\delta^{18}O$ and δD) of gypsum hydration water to ascertain the role of water condensation in the formation of subaerial gypsum speleothems. Chem. Geol. 452, 34–46.

Gázquez F., Morellón M., Bauska T., Herwartz D., Surma J., Moreno A., Staubwasser M., Valero-Garcés B., Delgado-Huertas A., Hodell D.A. 2018. Triple oxygen and hydrogen isotopes of gypsum hydration water for quantitative paleo-humidity reconstruction. Earth Planet. Sci. Lett. 481, 177–188.

Ginés A., Ginés. J. 2007. Eogenetic karst, glacioeustatic cave pools and anchialine environments on Mallorca Island: a discussion of coastal speleogenesis. Int. J. Speleol, 36, 57-67.

Gómez-Laserna, O, Olazabal, M.A, Morillas, H, Prieto-Taboada, N, Martinez-Arkarazo, I, Arana, G, Madariaga, J.M. 2013. In-situ spectroscopic assessment of the conservation state of building materials from a Palace house affected by infiltration water. J Raman Spectrosc. 44, 1277–1284.

Gomis-Yagües, V., Boluda-Botella, N. Ruiz-Bevia, F. 2000. Gypsum precipitation as an explanation for the decrease of sulfate concentration during seawater intrusion. J. Hydrol. 228, 48-55.

689 Gordillo, A., Espinosa, J., Martin, J.M., Pérez, A. 1972. Mapa Geológico
690   Cartagena. 1:50.000. IGME.

691 Goudie, A.S., Viles, H. A. 1997. Salt weathering. Chichester: Wiley, 241 pp.

692 Goudie, A.S., Day, M. J. 1980. Disintegration of fan sediments in Death Valley,
693   California, by salt weathering. Phys. Geogr. 1, 126-137.

694 Hodell, D.A., Turchyn, A.V., Wiseman, C.J., Escobar, J., Curtis, J.H., Brenner,
695   M., Gilli, A., Mueller, A.D., Anselmetti, F., Ariztegui, D., Brown, E.T. 2012. Late
696   glacial temperature and precipitation changes in the lowland Neotropics by
697   tandem measurement of $\delta^{18}O$ in biogenic carbonate and gypsum hydration
698   water. Geochim. Cosmochim. Acta 77, 352–368.

699 Jameson, R.A. 1991. Concept and classification of cave breakdown: An analysis
700   of patterns of collapse in Friars Hole Cave System, West Virginia, in Kastning,
701   E.H., Kastning, K.M. (eds.), Appalachian karst. National Speleological Society,
702   Huntsville, AL, p. 35-44.

703 Liu, T., Artacho, E., Gázquez, F., Walters, G., Hodell, D.A. 2018. Prediction of
704   Equilibrium Isotopic Fractionation of the Gypsum/Bassanite/Water System
705   using First-Principles Calculations, Geochim. Cosmochim. Acta. 244, 1-11.

706 Llamusí, J.L., Ingles, S., Ros, A., Rodríguez, A., Pérez, C. 1990. Cavidades
707   Submarinas del Cabo Tiñoso (Cartagena). Revista Caliza, 1, 24.

708 Lowry, D.C. Jennings, J.N. 1974. The Nullarbor karst Australia: Zeitschrift für
709   Geomorphologie. 18, 35-81.

710 Maltsev, V.A., Self, C.A. 1992. Cupp-Coutunn cave system, Turkmenia, Central
711   Asia. Proceedings of the University of Bristol Speleological Society 19: 117-
712   149.

713   Martín, D. 2004. Programa para el análisis por difracción de rayos X. Método en

714   Polvo (XPowder). Universidad de Granada.

715   McArthur, J., Howarth, R., Bailey, T. 2001. Strontium isotope stratigraphy:

716   LOWESS version 3: best fit to the marine Sr-isotope curve for 0–509 Ma and

717   accompanying look-up table for deriving numerical age. J. Geol.109 (2), 155–

718   170.

719   Metzger, J.G., David A. Fike, D.A., Osburn, G.R., Guo, C.J., Aadison, A.N. 2015.

720   The source of gypsum in Mammoth Cave, Kentucky. Geology. 43, 187–190.

721   Moore, D.G. 1954. Origin and development of sea caves. Nat. Speleol. Soc. Bull.

722   16, 71–76.

723   Mottershead, D.N. 1989. Rates and patterns of bedrock denudation by coastal

724   salt spray weathering: a seven-year record. Earth Surf. Process Landforms.

725   14, 383-398.

726   Mustoe, G. E. 1982. The origin of honeycomb weathering. Geol. Soc. Am. Bull.

727   93, 108-115.

728   Mylroie, J.E., Carew, J.L. 1990. The Flank Margin Model for Dissolution Cave

729   Development in Carbonate Platforms: Earth Surf. Process. Land. 15, 413-424.

730   Mylroie J.R, Mylroie J.E. 2007. Development of the carbonate island karst model.

731   J. Cave Karst Stud. 69(1), 59-75.

732   Natalicchio, M., Dela Pierre, F., Lugli, S., Lowenstein, T. K., Feiner, S. J.,

733   Ferrando, S., Manzi, V., Roveri, M. and Clari, P. 2014. Did Late Miocene

734   (Messinian) gypsum precipitate from evaporated marine brines? Insights from

735   the Piedmont Basin (Italy). Geology 42, 179–182.

736   Oerter, E., Singleton, M., Davisson, M. 2018. Hydrogen and oxygen stable
737   isotope dynamics of hyper-saline and salt-saturated aqueous solutions
738   Geochim. Cosmochim. Acta 238, 316-328.

739   Onac, B.P., Wynn, J.G., Sumrall, J.B. 2011. Tracing the sources of cave sulfates:
740   a unique case from Cerna Valley, Romania. Chem. Geol. 288, 105-114.

741   Pierre, C. 2018. The isotopic record of gypsum diagenesis in diluted solutions:
742   Observations in natural salinas and experiments. Chem. Geol. 493, 451-457.

743   Prebble, M.M. 1967. Cavernous weathering in the Taylor Dry Valley, Victoria
744   Land, Antarctica. Nature, 216, 1194-1195.

745   Puch, C, 1998. Grandes Cuevas y simas de España, Barcelona pp. 781-782.

746   Raab, M., Spiro, B., 1991. Sulfur isotopic variations during seawater evaporation
747   with fractional crystallization. Chem. Geol. 86, 323-333.

748   Rodriguez-Navarro, C.E., Doehne, E. 1999. Salt weathering: influence of
749   evaporation rate, supersaturation and crystallization pattern. Earth Surf.
750   Process Landforms 24, 191–209.

751   Sarrazin, P., Chipera, S., Bish, D., Blake, D., Vaniman, D. 2005. Vibrating sample
752   holder for XRD analysis with minimal sample preparation. International Centre
753   for Diffraction Data. Adv. X-ray Anal. 48, 156–164.

754   Sim, M.S., Bosak, T., Ono, S. 2011. Large sulfur isotope fractionation does not
755   require disproportionation. Science 333, 74–77.

756   Sofer, A. 1978. Isotopic composition of hydration water of gypsum. Geochim.
757   Cosmochim. Acta 42, 1141-1149.

758   Van Driessche, A.E.S., Canals, A., Ossorio, M., Reyes, R.C., García-Ruiz, J.M.
759   2016. Unraveling the sulfate sources of (giant) gypsum crystals using gypsum
760   isotope fractionation factors. J. Geol. 124, 235-245.

761   Van Stempvoort, D.R., Krouse, H.R. 1994. Controls of sulfate $\delta^{18}O$: a general

762   model and application to specific environments. In: Alpers, C., Blowes, D.

763   (Eds.), Environmental Geochemistry of Sulfide Oxidation. American Chemical

764   Society Symposium Series, 550, 446–480.

765   Wexler, A., Hasegawa, S. 1954. Relative humidity-temperature relationships of

766   some saturated salt solutions in the temperature range $0\,^{\circ}C$ to $50\,^{\circ}C$. J. Res.

767   Natl. Bur. Stand, 53, 19, RP 2512.

768   White, W.B., White, E.L. 2003. Gypsum wedging and cavern breakdown: Studies

769   in the Mammoth Cave System, Kentucky: Journal of Caves and Karst Studies.

770   65, 43–52.

771   Zerkle, A.L., Jones, D.S., Farquhar, J., Macalady J.L. 2016. Sulfur isotope values

772   in the sulfidic Frasassi cave system, central Italy: a case study of a

773   chemolithotrophic S based ecosystem Geochim. Cosmochim. Acta 173, 373-

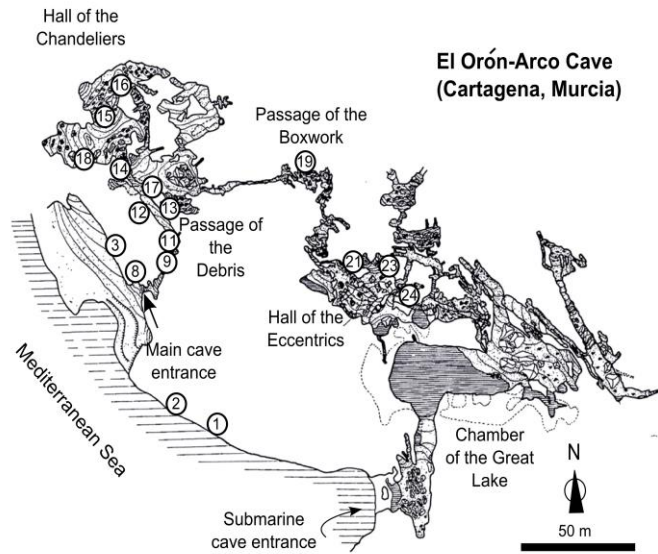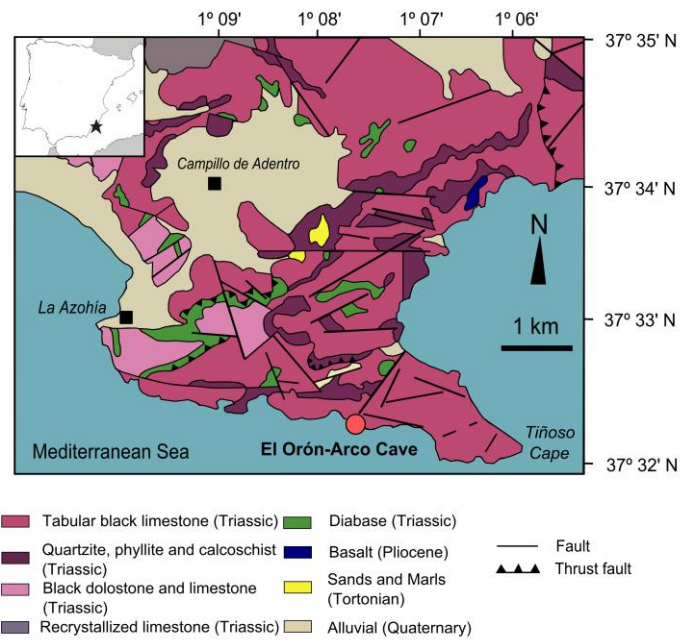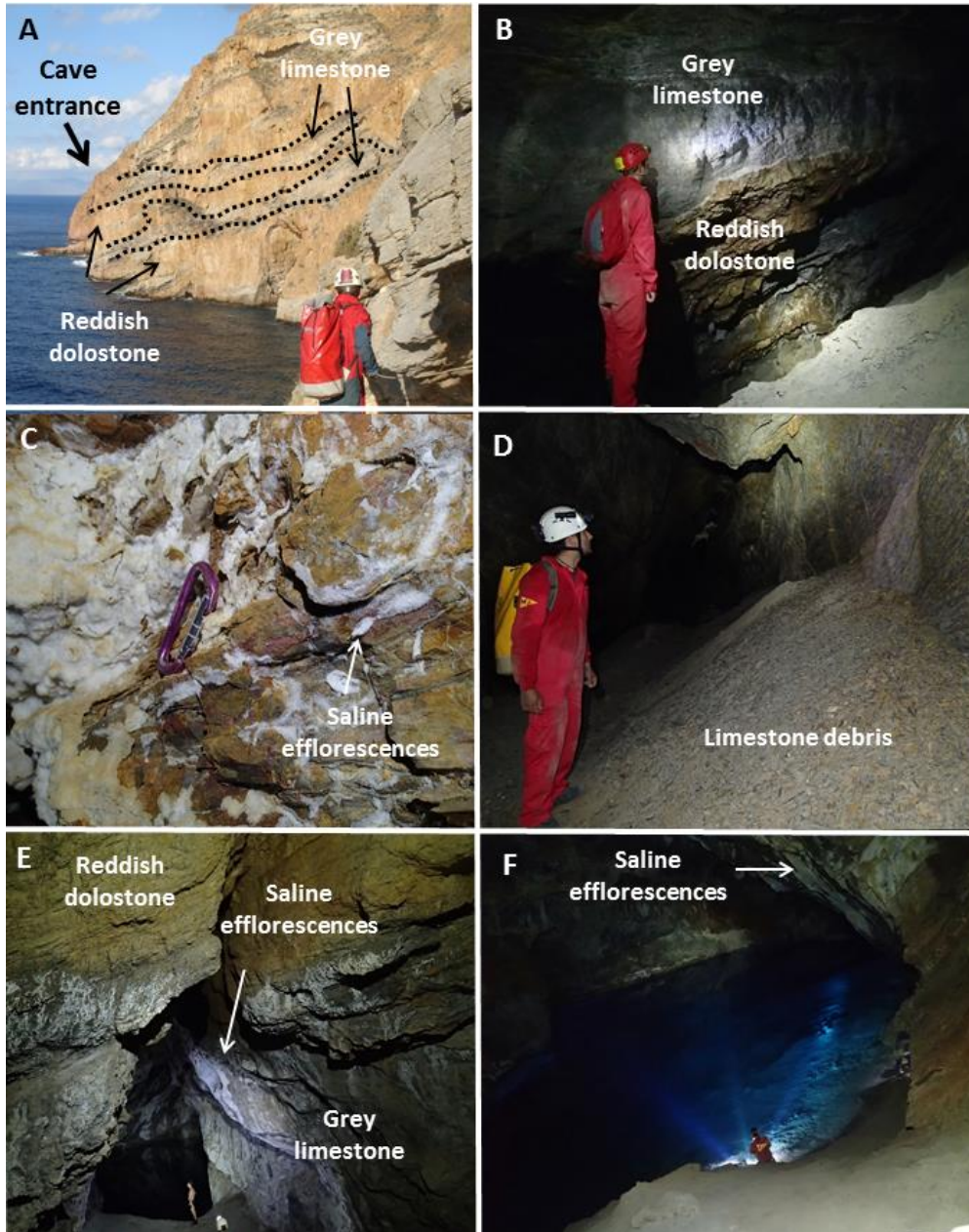774   386.

775

776

777

778

779

780

781

782

783

784

785

FIGURES AND TABLES CAPTIONS

Figure 1. Geological setting of Cabo Tiñoso (after Gordillo *et al.,* 1972) and

topography of El Orón-Arco Cave (produced by Llamusí, Inglés and Ros, 1984-

1998). Sampling sites are indicated.

794

Figure 2. A. Interbedded highly foliated greyish limestones and reddish dolostone in which El Orón-Arco Cave is hosted; **B**. Contact between the limestones and the dolostone inside the cave; **C**. Saline concretions on the cave walls. **D**. Piles of unsorted rock fragments on the cave walls; **E**. Altered limestone and saline concretions; **F**. Saline efflorescences on the walls of the Hall of the Great Lake.

800
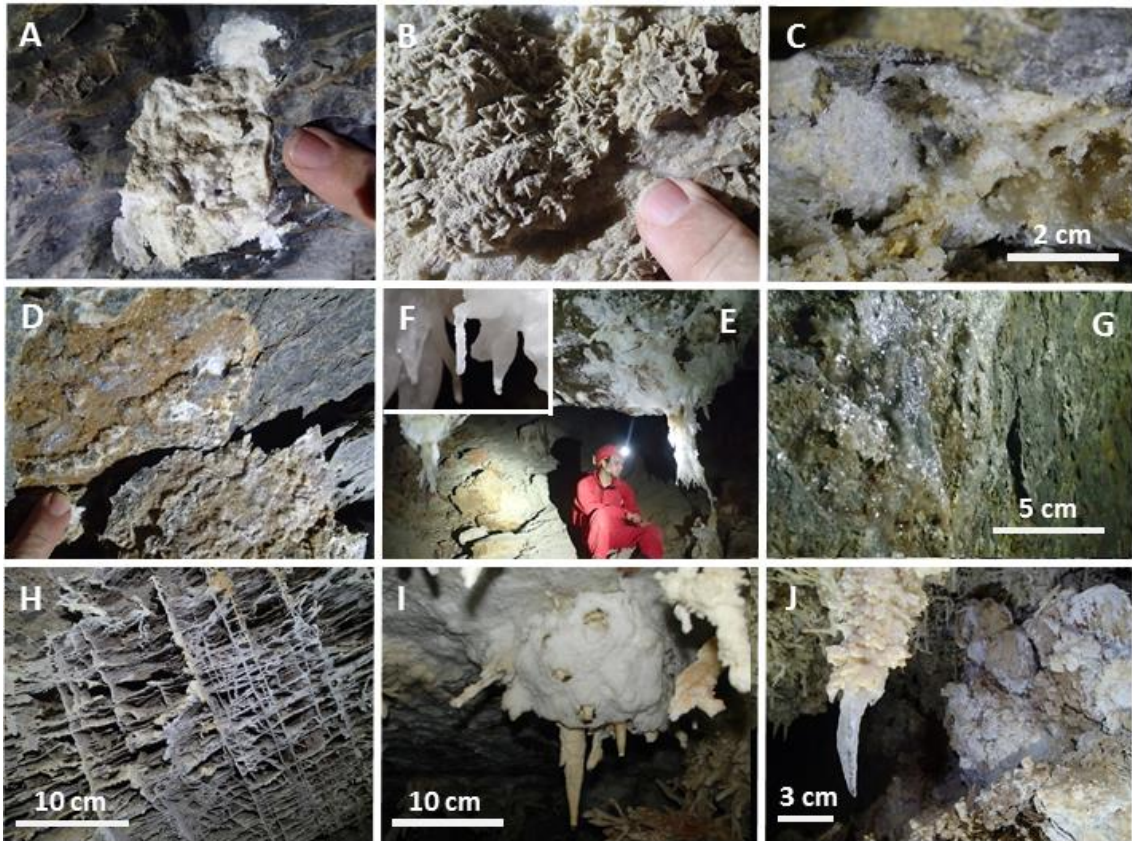
Figure 3. Speleothems in El Orón-Arco Cave: **A**. Concretions of gypsum on the carbonate host-rock; **B**. Aggregate of gypsum crystals covered by sandy materials; **C**. Saline concretions (gypsum + halite) in planes of the host-rock; **D**. Sugar-textured calcite infillings in planes of the host-rock; **E**. Gypsum 'chandeliers'; **F**. Details of the apex of a 'chandelier'; **G**. Saline coating on the cave walls; **H**. Carbonate boxwork formations covered with microcrystalline gypsum; **I**. Hollow gypsum hemispheres ('blisters') surrounded by carbonate eccentrics; **J**. Gypsum single crystals hanging from the tip of a carbonate dripstone.
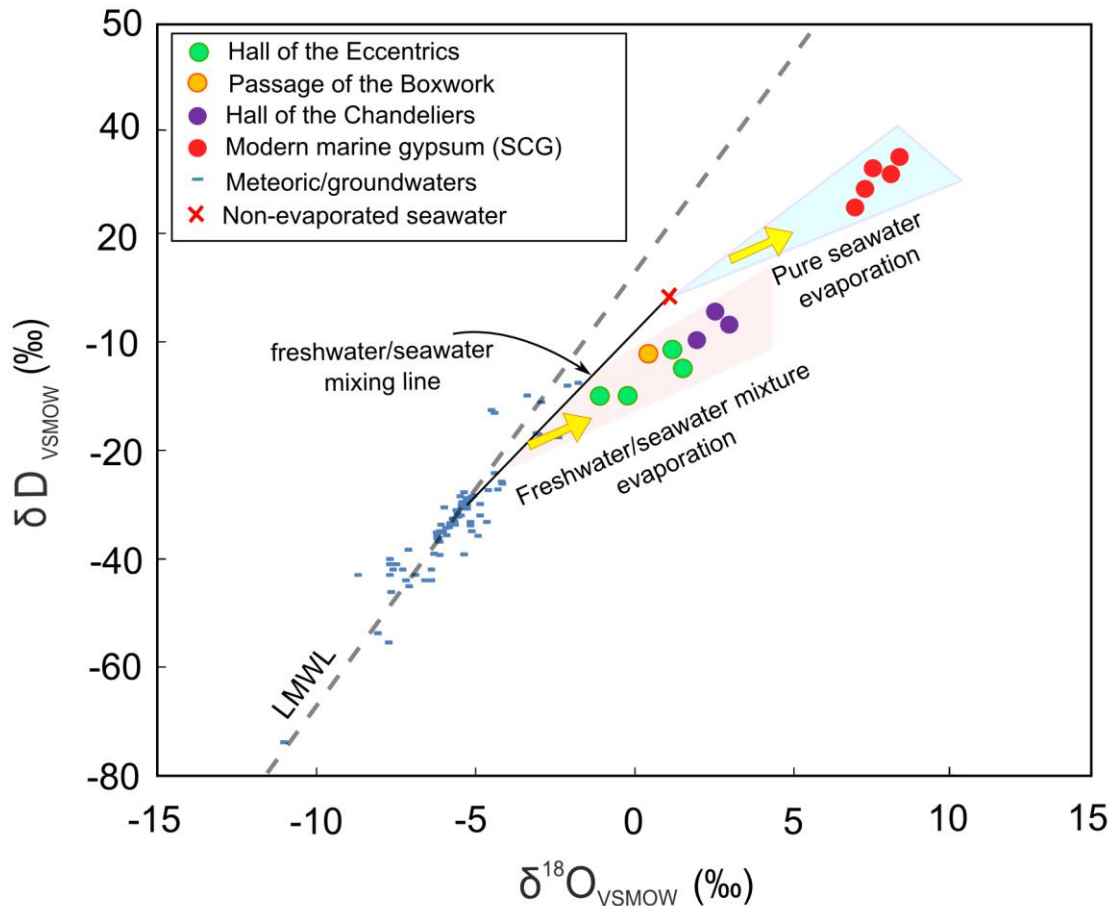
812
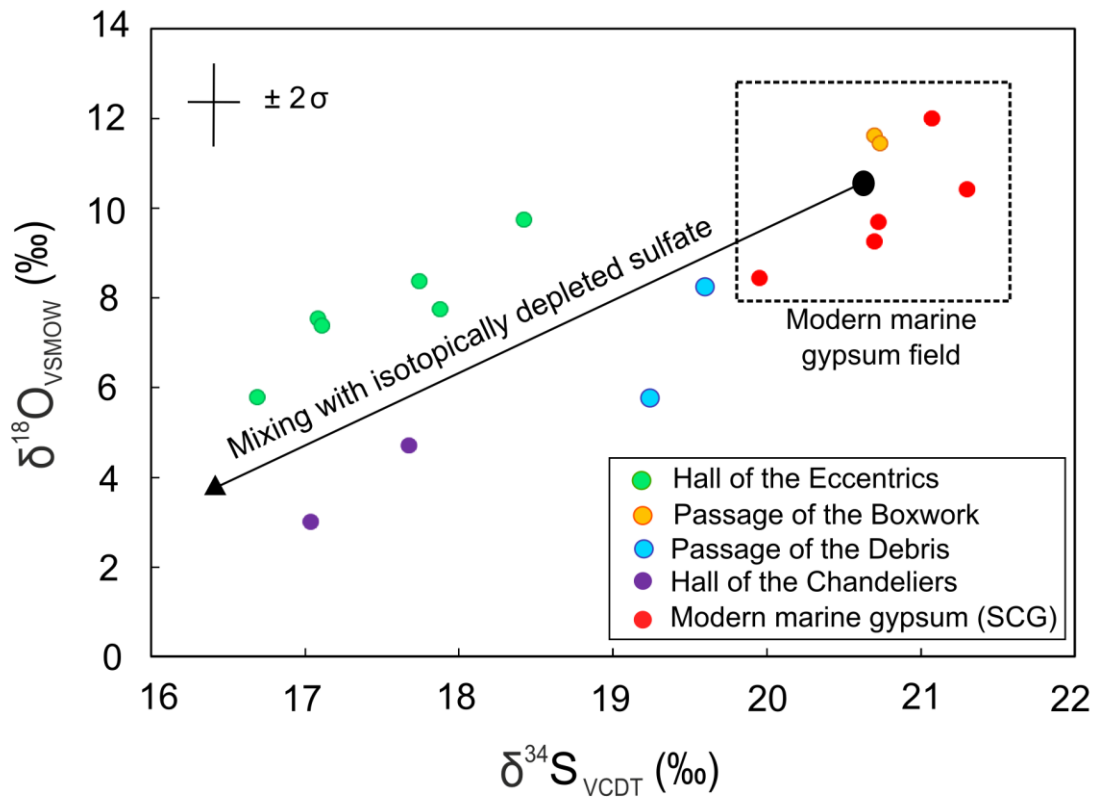
Figure 4. Sulfur and oxygen isotope composition of gypsum speleothems from El Orón-Arco Cave. The $\delta^{34}S$ and $\delta^{18}O_{SO4}$ values of modern marine gypsum (SCG samples) from a nearby salt factory (Salina of Cabo de Gata, Almeria, SE Spain; Evans et al., 2015) are presented for comparison.

817

Figure 5. Oxygen and hydrogen isotopes of speleothem-forming water in El Orón-Arco Cave obtained from gypsum hydration water after applying known isotope fractionation factors by Gázquez et al. (2017a) (see main text). Isotope composition of meteoric and groundwaters in SE Spain are given for comparison (Gázquez et al., 2017b), as well as the mother water from which marine gypsum formed in a nearby salt factory (Salina of Cabo de Gata, Almeria, SE Spain; Evans et al., 2015; Gazquez et al., 2017a). Analytical errors are smaller than the symbols.

826
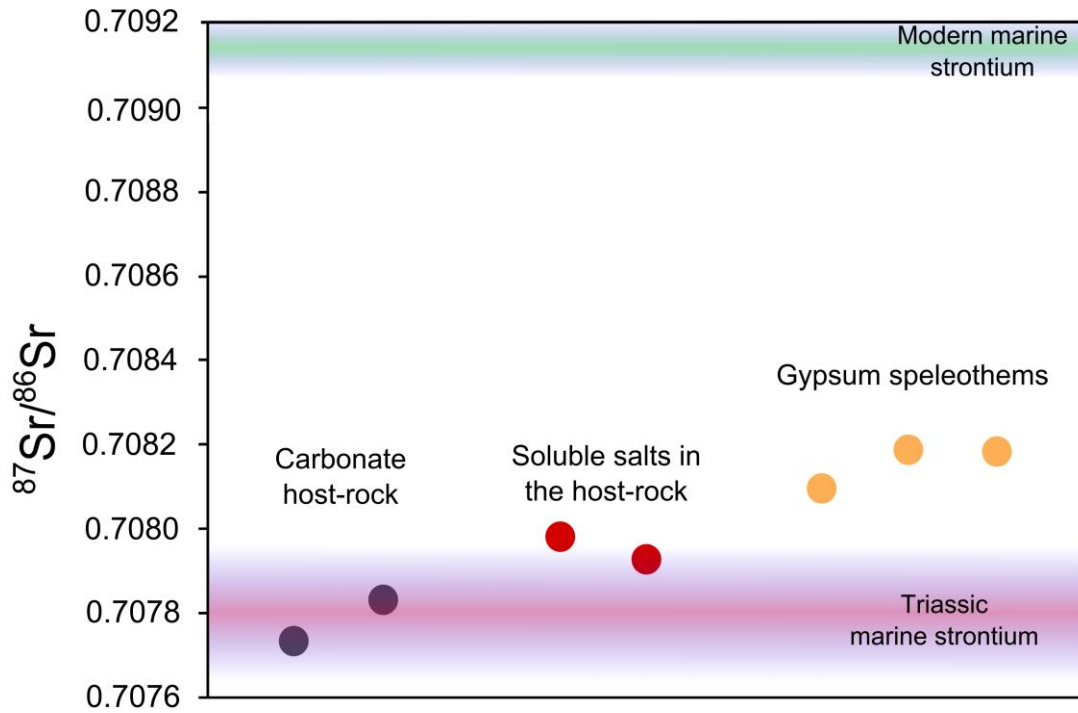
Figure 6. Strontium isotope composition ($^{87}Sr/^{86}Sr$) of gypsum speleothems, carbonate host-rock and soluble salts leached from the host-rock in El Orón-Arco Cave. Analytical errors are smaller than the symbols.

830
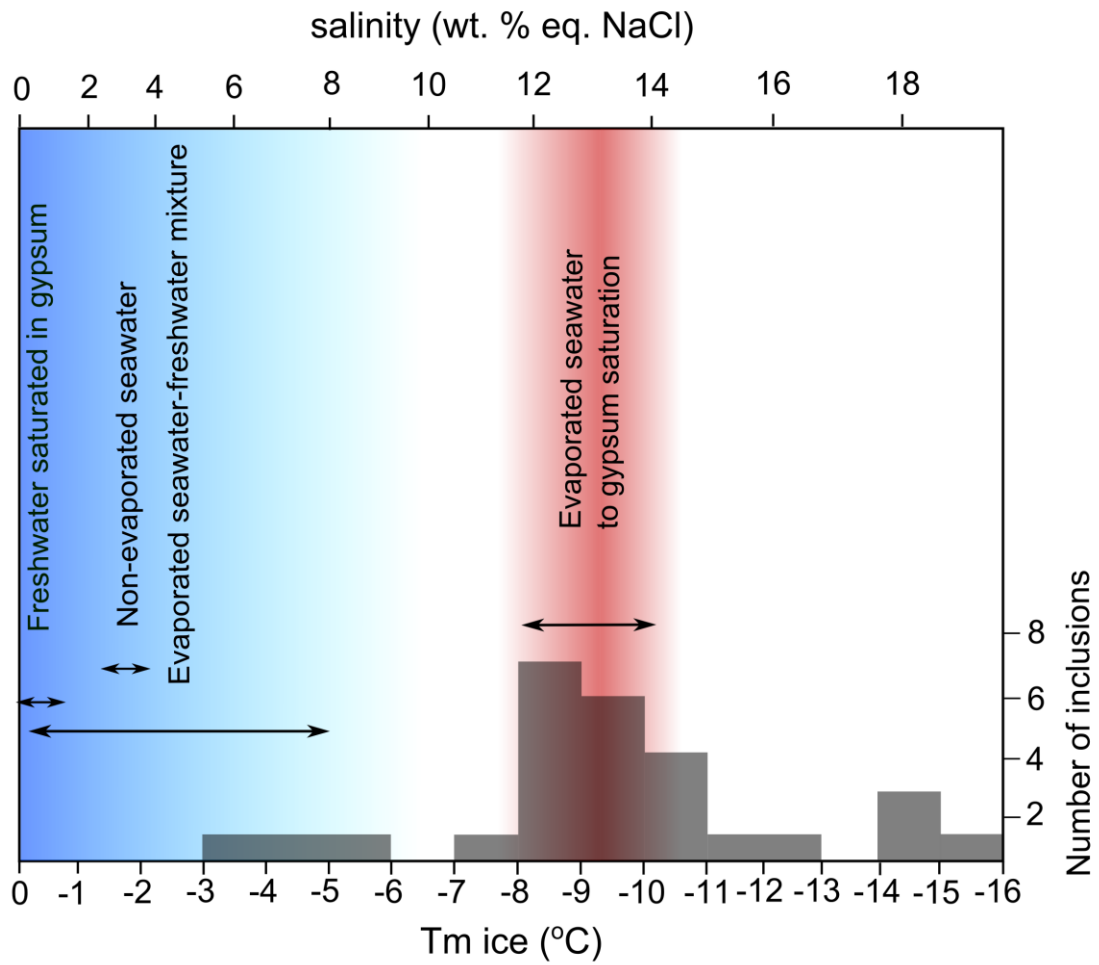
Figure 7. Microthermometry of primary fluid inclusions in gypsum speleothems from El Orón-Arco Cave. Ice melt temperature (T_m) of fluid inclusions were converted to salinity (wt. % eq. NaCl) using the equation of Bodnar (1993).

834
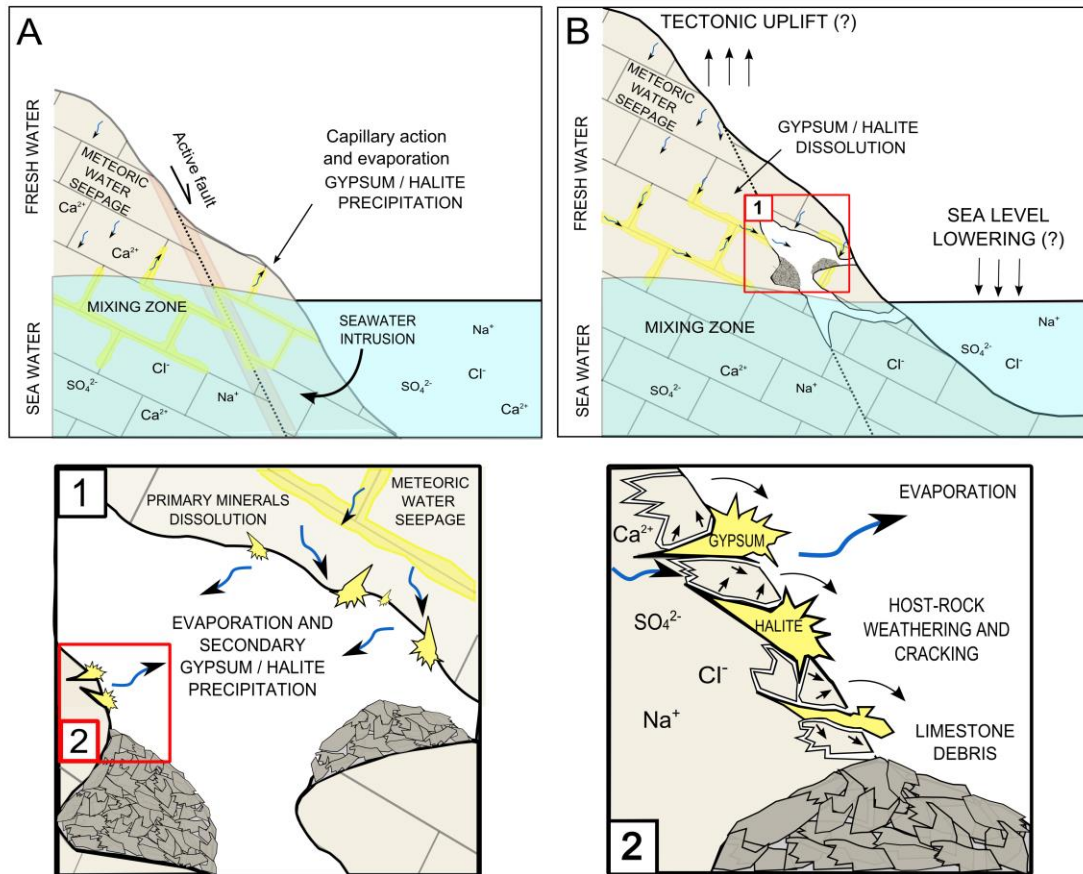
Figure 8. Conceptual sketch of the mechanism that formed El Orón-Arco Cave: **A**. Seawater intrusion and capillary action of brackish water that evaporates in voids of the host-rock, leading to primary evaporites (mostly gypsum and halite) precipitation and carbonate weathering; **B**. Enhanced saline weathering by sea salts precipitation with greater contribution of meteoric water seepage and dissolution of primary evaporites in subaerial conditions, resulting in precipitation of secondary evaporites, host-rock cracking and accumulation of debris detached from the cave walls. Panels 1 and 2 are zooms of panel B, showing the idealized weathering process. Note that faulting and tectonics may have also had a significant role during the formation of the cave and meteoric water flow thought the carbonate host-rock, particularly during its initial genetic stages.

846

Sample	Description	Site	Mineralogy	$\delta^{34}S_{SO4}$	$\delta^{18}O_{SO4}$	$\delta^{18}O_{GHW}$	δD_{GHW}	$\delta^{18}O_{MW}$	δD_{MW}	Th (°C)	% NaCl eq	$^{87}Sr/^{86}Sr$
CT-01	Yellowish calcschist	Outside	Calcite	-	-	-	-	-	-	-	-	
CT-02	Grey host-rock	Outside	Calcite	-	-	-	-	-	-	-	-	
CT-03	Infillings along host-rock strata	Outside	Halite, gypsum (-)	-	-	-	-	-	-	-	-	
CT-08	Grey limestone	Outside	Calcite, dolomite (-)	-	-	-	-	-	-	-	-	0.707737 (0.707988)
CT-09	Whitish coating on host-rock	Entrance passage	Gypsum	17.7	8.4	-	-	-	-	-	-	
CT-11	Gypsum 'rose' in sediment	Entrance passage	Gypsum	19.6	8.3	-	-	-	-	-	-	
CT-12	Sugary texture brownish infillings	Passage of the debris	Calcite, dolomite (-)									
CT-13	Crystalline coatings on the cave wall	Passage of the debris	Gypsum, celestine (-)	19.2	5.8	-	-	-	-	-	-	0.708188
CT-14	Reddish host-rock	Hall of the Chandeliers	Dolomite, goethite (-)									
CT-15A	Microcrystalline coatings over chandeliers	Hall of the Chandeliers	Gypsum	17.0	-	5.5	-16.9	2.2	3.2	-	-	
CT-15B	Gypsum chandelier (1)	Hall of the Chandeliers	Gypsum	17.7	4.7	5.8	-13.6	2.5	1.4	-10.7±2.5	14.2±2.5	0.708183
CT-15C	Halite soda-straw	Hall of the Chandeliers	Halite, celestine (-)	-	-	-	-	-	-	-	-	
CT-16	Gypsum chandelier (2)	Hall of the Chandeliers	Gypsum	17.0	3.0	4.8	-16.9	1.5	-2.0	-	-	
CT-17	Microcrystalline gypsum	Passage of the debris	Gypsum	17.1	7.5	4.3	-21.4	1.0	-6.5	-	-	
CT-18A	Yellowish powder in planes of the host-rock	Hall of the Chandeliers	Halite, gypsum, quartz (-)	17.0	-	-	-	-	-	-	-	
CT-18B	Reddish host-rock	Hall of the Chandeliers	Dolomite, goethite (-)	-	-	-	-	-	-	-	-	0.707835 (0.707926)
CT-18D	Whitish veins in the host-rock	Hall of the Chandeliers	Calcite	-	-	-	-	-	-	-	-	
CT-19A	Whitish coatings on boxwork	Hall of the Boxwork	Gypsum	20.7	11.6	3.4	-18.9	0.1	-4.0	-	-	
CT-19B	Boxwork laminae	Hall of the Boxwork	Dolomite, calcite (-)	-	-	-	-	-	-	-	-	
CT-21B	Stalactite	Hall of the Eccentrics	Aragonite	-	-	-	-	-	-	-	-	
CT-21A	Spar on the tip of a stalactite	Hall of the Eccentrics	Gypsum	16.7	5.8	4.1	-18.8	0.8	-3.9	-9.9±2.4	13.3±2.4	
CT-21C	'Blister' speleothem (1)	Hall of the Eccentrics	Gypsum	17.1	7.4	2.6	-24.8	-0.7	-9.9	-	-	0.708095
CT-23A	Microcrystalline coating over stalactite	Hall of the Eccentrics	Gypsum	18.4	9.8	-	-	-	-	-	-	
CT-23A1	Spar on the tip of a stalactite	Hall of the Eccentrics	Gypsum	-	-	-	-	-	-	-5.3±1.9	8.2±2.6	
CT-23B	Stalactite	Hall of the Eccentrics	Aragonite	-	-	-	-	-	-	-	-	
CT-23C	Stalactite	Hall of the Eccentrics	Aragonite	-	-	-	-	-	-	-	-	
CT-24	'Blister' speleothem (2)	Hall of the Eccentrics	Gypsum	17.9	7.8	2.0	-24.7	-2.3	-9.9	-	-	

847 **Table 1.** Mineralogical and geochemical analyses of samples from El Orón-Arco Cave. Results of $\delta^{18}O$ and $\delta^{34}S$ in sulfate, $\delta^{18}O$ and δD in gypsum
848 hydration water (GHW) and strontium isotopes ($^{87}Sr/^{86}Sr$) are presented. $^{87}Sr/^{86}Sr$ in brackets correspond to leaches from the carbonate host-
849 rock. The $\delta^{18}O$ and δD of gypsum mother water (MW) have been reconstructed by applying fractionation factors by Gázquez et al. (2017a). Ice
850 melt temperatures of primary fluid inclusions (Tm) in gypsum speleothems and derived salinities (wt. % NaCl eq.) calculated from the equation
851 of Bodnar (1993), are also given